Microchimica Acta (2024) 191:450
https://doi.org/10.1007/s00604-024-06530-x

ORIGINAL PAPER

Spatially confined dual-emission nanoprobes assembled from silicon nanoparticles and gold nanoclusters for ratiometric biosensing

Weiheng Kong[1,2] · Jiahao Li[1] · Yuntian Yan[1] · Qingqing Tan[2] · Rong-mei Kong[1] · Meihao Xiang[1] · Ensheng Zhang[1] · Yan Zhao[1,2]

Received: 11 April 2024 / Accepted: 26 June 2024 / Published online: 6 July 2024

Abstract

Gold nanoclusters (AuNCs) possess weak intrinsic fluorescence, limiting their sensitivity in biosensing applications. This study addresses these limitations by developing a spatially confined dual-emission nanoprobe composed of silicon nanoparticles (SiNPs) and AuNCs. This amplified and stabilized fluorescence mechanism overcomes the limitations associated with using AuNCs alone, achieving superior sensitivity in the sensing platform. The nanoprobe was successfully employed for ratiometric detection of bleomycin (BLM) in serum samples, operating at an excitation wavelength of 365 nm, with emission wavelengths at 480 nm and 580 nm. The analytical performance of the system is distinguished by a linear detection range of 0–3.5 μM, an impressive limit of detection (LOD) of 35.27 nM, and exceptional recoveries ranging from 96.80 to 105.9%. This innovative approach significantly enhances the applicability and reliability of AuNC-based biosensing in complex biological media, highlighting its superior analytical capabilities.

Keywords Gold nanoclusters · Aggregated emission enhancement · Dual-emission nanoprobes · Ratiometric biosensing · Spatial confinement

Introduction

Gold nanoclusters (AuNCs) are classic fluorescent nanomaterials comprised of dozens of gold atoms [1]. In recent years, AuNCs have found widespread application as fluorescent probes for detecting various biomarkers [2, 3]. Compared to traditional organic dyes and semiconductor quantum dots, AuNCs possess smaller sizes, superior biocompatibility, and more photostable fluorescence, enabling highly selective detection of trace biomolecules [3, 4]. While AuNCs have demonstrated considerable potential for application in biosensing, their inherently weak fluorescence signals also impose limitations on further improvements to the sensitivity of AuNC-based sensing platforms [5]. The aggregation emission enhancement (AEE) mechanism provides a possible breakthrough to address this problem with AuNC-based biosensors [6, 7]. The AEE effect, also known as the aggregation-induced emission enhancement (AIEE) effect, enhances the fluorescence emission intensity and increases the fluorescence quantum yield of AuNCs by inducing AuNC aggregation [8]. Therefore, developing novel strategies to precisely control the AEE process for efficient fluorescence enhancement is critically important. Additionally, elucidating the key factors governing the emission performance of AuNCs during the AEE process represents another vital research direction.

To date, various approaches to induce AEE effect have been explored, including modulation of pH [9], organic solvents [10], macromolecule/ion-mediated aggregation [11–13], and spatial confinement [14–17]. While the AEE mechanism presents opportunities to enhance AuNCs fluorescence, substantial limitations persist regarding the direct application of AuNCs as biosensing elements and their use in intricate biological systems [7, 16]. For one thing, actual samples contain a myriad of biomolecules, and introducing additional organic reagents or materials may alter sample properties and introduce uncontrolled interferences. For

✉ Yan Zhao
yanzhao2016@hnu.edu.cn

[1] Key Laboratory of Life-Organic Analysis of Shandong Province, School of Chemistry and Chemical Engineering, Qufu Normal University, Qufu, P. R. China

[2] State Key Laboratory of Chemo/Biosensing and Chemometrics, Hunan University, Changsha 410082, P. R. China

another, numerous assays necessitate mild physiological pH conditions to maintain the stability of certain proteases in bodily fluids [18]. In light of these considerations, spatial confinement effects offer a straightforward method to regulate the AEE process of AuNCs, which can be leveraged to construct robust biosensing systems through modulating the AEE mechanism without altering the essential conditions of samples [19, 20]. This approach also addresses the deficiencies of AuNCs such as low fluorescence intensity, small threshold for signal change, and poor sensitivity and detection limits [21]. Importantly, the aggregation of AuNCs can be readily controlled and spatially confined through approaches such as electrostatic interactions [22]. The negatively charged ligand-protected AuNCs can be assembled with positively charged molecules/particles via electrostatic interactions, stabilizing the AuNCs in a confined state and reducing radiative transitions of the AuNCs, thereby enhancing fluorescence.

However, several aspects of AuNC aggregation mediated by electrostatic interactions remain poorly defined. First, the influence of surface charge density on AEE is unclear, generally, greater surface charge density promotes more robust electrostatic interactions [23, 24]. Nevertheless, systematic studies elucidating the effects of varying surface charge densities on the AEE phenomenon are lacking. Second, research is limited regarding the proximity of aggregation between AuNCs; tighter inter-AuNC distances strengthen spatial confinement but may also exacerbate fluorescence quenching [3, 25, 26]. Defining the optimal degree of aggregation closeness at the physical level remains an outstanding challenge. Finally, interactions between neighboring aggregates/ligands are still ill-defined, with restricted vibration/rotation of ligands thought to contribute to AEE; however, further characterization of inter-ligand interactions between adjoining AuNCs is warranted [27, 28]. Numerous facets of the AEE mechanism induced by spatial confinement require in-depth investigation. Considering the need to account for the magnitude of fluorescence intensity and range of fluorescence signal changes when constructing AuNC-based sensing systems, the utilization of judicious characterization and modeling approaches will likely illuminate these unclear mechanisms.

In this work, we constructed three models of AuNCs exhibiting AEE through spatial confinement. Loose surface charge AuNC aggregates were generated by assembling L-arginine (L-Arg) with AuNCs via electrostatic interactions. PVP was stirred and assembled with AuNCs, forming AuNCs aggregates with loose inter-particle spacing by wrapping and entanglement. Silicon nanoparticles (SiNPs) were mixed with AuNCs, triggering agglomeration based on the dual effects of electrostatic interactions and spatially constrained aggregation, thereby inducing the AEE effect. Through constructing and characterizing these three models, we optimized and obtained the most suitable SiNP-AuNC nanoprobes for biosensing systems. The SiNP-AuNC nanoprobes not only optimized conditions conducive to the AEE strategy under spatial confinement but also enabled ratiometric detection, which could effectively minimize environmental fluctuations by taking the ratio of the dual emission peak intensities, improving detection stability. Further, to validate the application potential of SiNP-AuNC nanoprobes in biosensing, the probes were utilized for selective detection of bleomycin (BLM). The fluorescence-enhanced AuNCs constituted the sensing element while the SiNPs furnished a stable internal reference signal. Under optimized conditions, the probes exhibited dual emission peaks in which the AuNC peak intensity responded to changes in target concentration, while the SiNP signal remained constant, thereby eliminating matrix effects through the dual-peak ratio. In summary, the successful development of these AEE-enhanced dual-emission ratiometric fluorescent probes had overcome multiple limitations of AuNC-based sensors for application in intricate biological systems and achieved excellent sensitivity and detection limits. This study provided a novel approach to implementing the AEE strategy under spatial confinement for expanding AuNC applications in biological sample analysis.

Experimental

Materials and instruments

All the details of materials and instruments were shown in Supporting Information.

Preparation of SiNPs, AuNCs, SiNPs-AuNCs, Arg-AuNCs, and PVP-AuNCs

The detailed information for synthesis was presented in Supporting Information.

Feasibility study of the dual-emission ratiometric fluorescence detection assay

To evaluate the feasibility of the dual-emission ratiometric fluorescence detection assay, we conducted detailed experiments using SiNPs, AuNCs, and SiNPs-AuNCs. The fluorescence spectra were measured under different conditions to assess the stability and sensitivity of the detection system. SiNPs-AuNCs were prepared by mixing the synthesized SiNPs and AuNCs at a mass ratio of 10:1 to ensure optimal binding and fluorescence properties. The fluorescence spectra of SiNPs, AuNCs, and SiNPs-AuNCs were recorded in the presence and absence of Cu^{2+} ions and/or BLM. We prepared

a series of Cu^{2+} solutions (200 μM) and BLM solutions of various concentrations to test the response of the dual-emission system. For each measurement, 100 μL of Cu^{2+} solution and 100 μL of BLM solution (at different concentrations) were added to 700 μL of PBS buffer (10 mM, pH 7.4). After equilibration at room temperature for 10 min, 100 μL of SiNP-AuNC solution was added to the mixture. The fluorescence spectra were measured using a fluorescence spectrophotometer with an excitation wavelength of 365 nm.

Detection of BLM

For BLM detection, 100 μL of Cu^{2+} solution (200 μM), 100 μL of BLM solutions of various concentrations, and 700 μL of PBS buffer (10 mM, pH 7.4) were equilibrated at room temperature for 10 min. Then, 100 μL of SiNP-AuNC solution was added to the mixture. The fluorescence spectra were measured at 365 nm excitation wavelength.

Interference and selectivity studies

To assess interference from metal ions, we tested the response of the SiNP-AuNC system to a range of metal ions, including Cu^{2+}, Na^{+}, K^{+}, Mg^{2+}, Al^{3+}, Ca^{2+}, Zn^{2+}, Hg^{2+}, Pb^{2+}, and Cd^{2+}. Each metal ion was tested at a concentration of 200 μM.

The selectivity of the SiNP-AuNC system was evaluated by testing its response to common biological small molecules, including dopamine, ascorbic acid, glucose, L-glutamic acid, aspartic acid, L-cysteine, L-tyrosine, L-histidine, and BLM. Each biological molecule was also tested at a concentration of 200 μM.

For both interference and selectivity studies, solutions of each metal ion and biological small molecule were prepared at a concentration of 200 μM. A Cu^{2+} solution (200 μM) was used as a reference quenching agent. In each test, 100 μL of Cu^{2+} solution (200 μM) and 100 μL of the corresponding metal ion or biological small molecule solution were mixed with 700 μL of PBS buffer (10 mM, pH 7.4). The mixtures were equilibrated at room temperature for 10 min to ensure proper interaction. After equilibration, 100 μL of SiNPs-AuNCs solution was added to each mixture. The final volume in each test was 1 mL. The fluorescence spectra were recorded using a fluorescence spectrophotometer with an excitation wavelength of 365 nm. The ratio of fluorescence intensities (F580/F480) was calculated to determine the ratiometric response of the sensing system. This ratio helps to mitigate any potential interference by providing a stable internal reference from the SiNPs.

Application of the SiNP-AuNC sensing system in real sample analysis

Serum samples were obtained from healthy individuals and provided by the school hospital of Qufu Normal University. All serum assay procedures were conducted in strict accordance with the guidelines established by the regional ethics committee for animal experiments at Qufu Normal University Institutional Animal Care and Use (2023026).

For the detection of BLM in serum samples, the analytical utility of the method was examined using spiked serum samples. Different concentrations of BLM (500 nM, 1500 nM, and 2500 nM) were added to the serum samples to assess the recovery and precision of the method. Briefly, 200 μL of each spiked serum sample was mixed with Cu^{2+} solution (final concentration 4 μM). The mixtures were equilibrated at room temperature for 10 min. Subsequently, 200 μL of the SiNP-AuNC solution was added to each mixture, and the fluorescence spectra were measured at an excitation wavelength of 365 nm.

The recovery of BLM was calculated using the following equation:

$$\text{Recovery}\ (\%) = (C - C0) \,/\, C_{\text{BLM}} \times 100\%$$

where C is the detected concentration of BLM in the spiked sample, C_0 is the original concentration of BLM in the unspiked sample, and C_{BLM} is the spiked concentration of BLM.

Statistical analysis

All experimental data were demonstrated as the mean with S.D. and were replicated 3 times in parallel under the same experimental conditions, unless otherwise specified.

Result and discussion

Construction and fluorescence properties investigation of AuNCs AEE model

Enhancing fluorescence intensity through AEE process was an effective approach to expand the performance of AuNC-based fluorescent sensors. Comprehensively considering the two classic mechanisms for achieving AEE in AuNCs, namely, electrostatic adsorption and spatial confinement, we constructed three AuNCs models with different assembly modes (Scheme 1). L-Arg-AuNCs aggregates with loose surface charge were generated by mixing negatively charged L-Arg and AuNCs via electrostatic interactions. PVP-AuNC aggregates with loose inter-particle spacing were formed

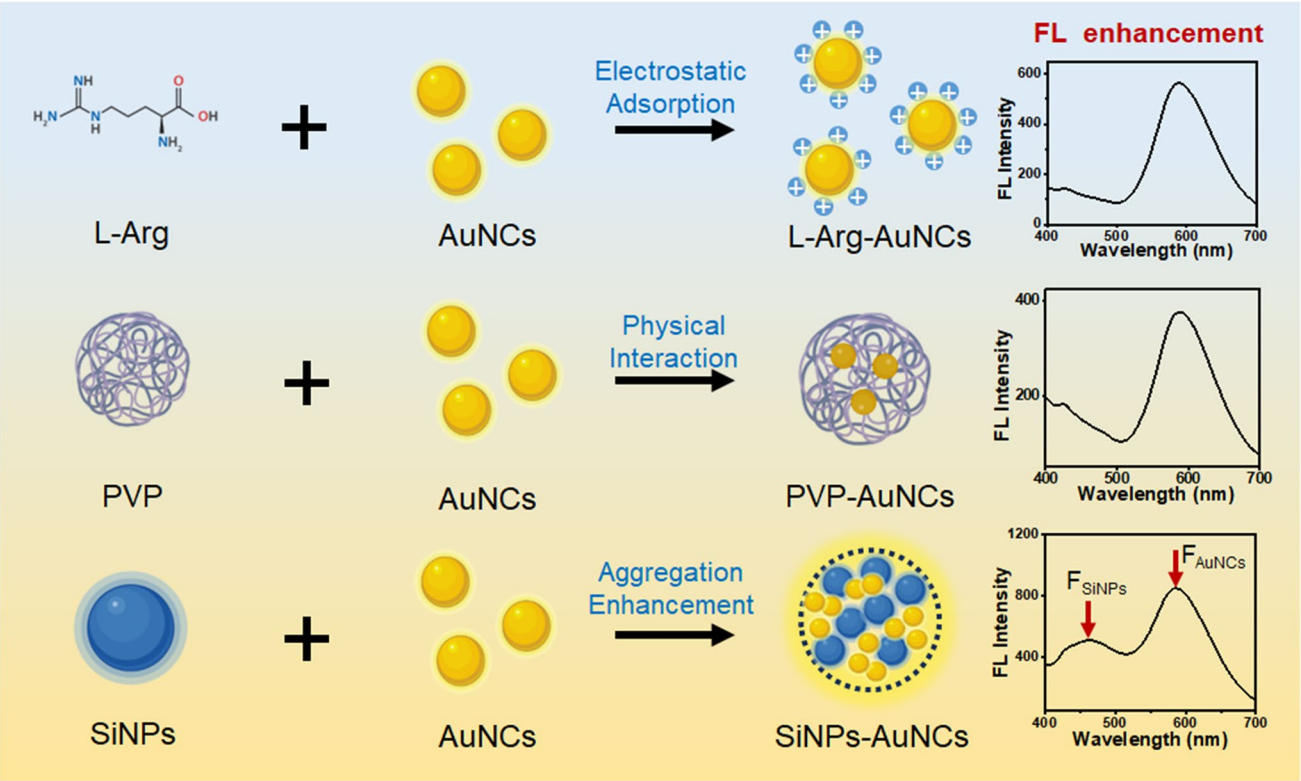

Scheme 1 The AEE study of AuNCs and the construction of spatially confined dual-emission nanoprobes assembled from SiNPs and AuNCs

by stirring PVP, a long-chain polymer, with AuNCs, which induced aggregation through wrapping and entanglement. SiNPs-AuNCs were prepared by mixing positively charged SiNPs with AuNCs, triggering aggregation based on the dual effects of electrostatic interactions and spatial confinement, thereby inducing the AEE effect.

After constructing the three models, we first characterized the fluorescence properties of AuNCs at the maximum emission peak of 580 nm. As expected, the fluorescence intensity of SiNPs-AuNC nanoparticles exhibited a significant enhancement. As shown in Fig. 1a, upon the addition of SiNPs (SiNPs:AuNCs, $m/m = 3{:}1$), the maximum fluorescence emission peak of AuNCs immediately displayed more than a two-fold enhancement. As the mass ratio of SiNPs to AuNCs further increased (gradually increasing from 3:1 to 20:1), the maximum emission peak of AuNCs maintained an enhancing trend (Fig. 1b, Fig. S1). It is noteworthy that even with the addition of high concentrations of SiNPs, the fluorescence emission peak of AuNCs remained well-preserved (Fig. S1), demonstrating the superiority of SiNPs for enhancing the AEE effect of AuNCs.

In contrast to the above model, we characterized the fluorescence properties of L-Arg-AuNCs constructed based on electrostatic interactions. After mixing with L-Arg, only a limited increase in the maximum fluorescence intensity of AuNCs was observed, with negative red-shift or blue-shift in the maximum emission wavelength of AuNCs (Fig. 1c, d and Fig. S2a). Notably, as the amount of L-Arg increased, the maximum fluorescence intensity exhibited negligible changes. Evidently, merely regulating positive charges in the system did not significantly alter the fluorescence performance of AuNCs. Interestingly, previous literature had reported that the cationic polypeptide polyarginine (polyArg) can effectively induce the AIEE of GSH-AuNCs [29]. To further verify whether the source of fluorescence enhancement stems from cations or the action of polymers, we introduced the long-chain polymer PVP into AuNCs, forming PVP-AuNC aggregates through wrapping and entanglement. The results showed that compared to AuNCs alone (Fig. S2b), the maximum fluorescence emission peak remained at 580 nm, with the maximum fluorescence intensity slightly decreasing (Fig. 1e, f). It was speculated that this might be due to the non-tight binding state of AuNCs in the aggregates, which were more likely in a loose aggregation state, unable to effectively achieve AEE. Additionally, PVP might also absorb a portion of the excitation light energy, leading to a reduction in fluorescence intensity. In summary, the generation of this AEE fluorescence was neither solely influenced by external charge nor enhanced by the physical wrapping/encapsulation effect of long-chain polymers. In contrast to the above phenomena, the fluorescence intensity of the tightly aggregated SiNP-AuNC nanoparticles based

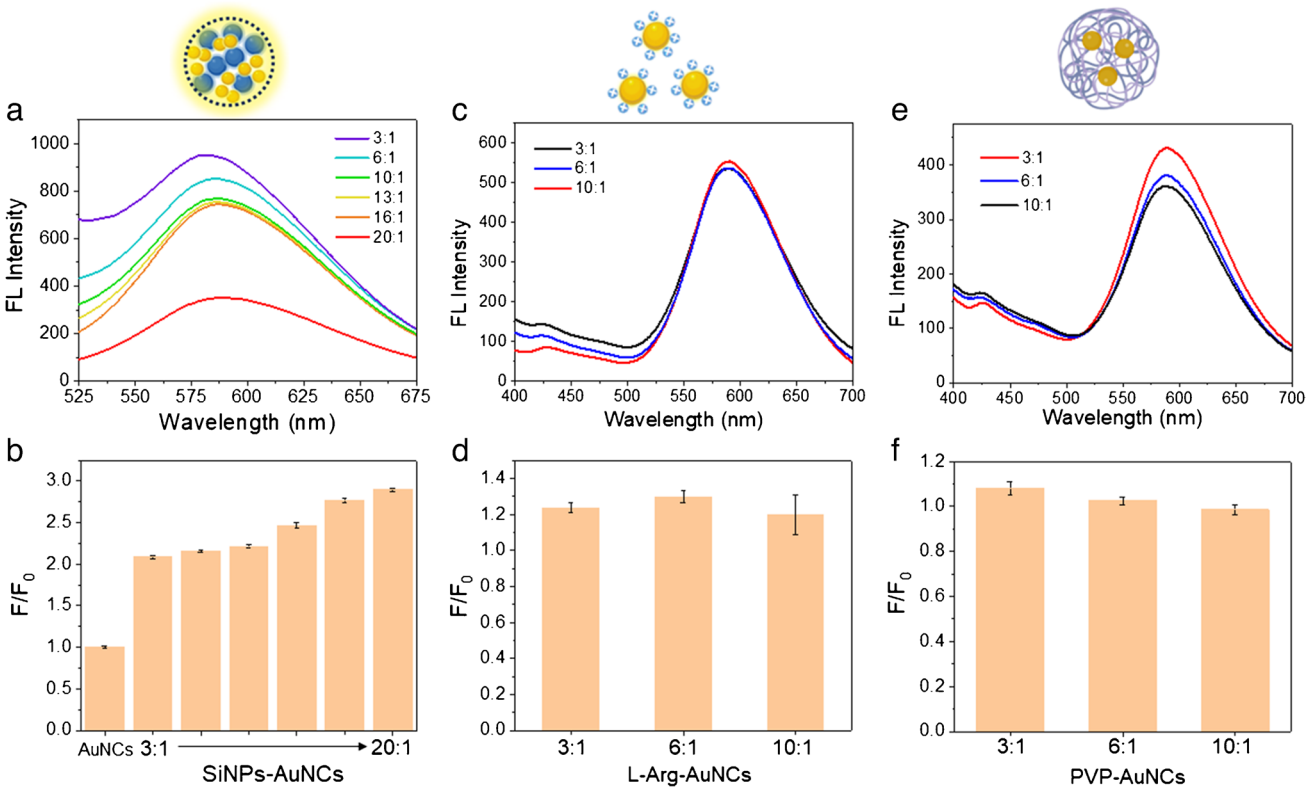

Fig. 1 **a** Fluorescence spectra of AuNCs in SiNPs-AuNCs and **b** the corresponding quantitative histograms of fluorescence intensity. **c** Fluorescence spectra of L-Arg-AuNCs and **d** the corresponding quantitative histograms of fluorescence intensity. **e** Fluorescence spectra of PVP-AuNCs and **f** the corresponding quantitative histograms of fluorescence intensity. F represents the fluorescence intensity at 580 nm in the mixed system, while F_0 represents the fluorescence intensity of AuNCs at 580 nm

on electrostatic interactions was enhanced, emphasizing the importance of controlling the tight aggregation of AuNCs in confined spaces during the AEE process.

Characterization and fluorescence enhancement mechanism of the SiNP-AuNC nanoprobes

To elucidate the assembly modes of L-Arg-AuNCs, PVP-AuNCs, and SiNPs-AuNCs, we conducted TEM characterization. As anticipated, L-Arg-AuNCs remained dispersed without any noticeable aggregation (Fig. S3a). The TEM images of PVP-AuNCs revealed that, under the influence of the long-chain polymer, AuNCs maintained a loosely aggregated state through physical entanglement (Fig. S3b, c). The assembly of SiNPs-AuNCs nanoparticles was based on the synergistic effects of electrostatic interactions between oppositely charged components and spatial aggregation (Fig. 2a). To confirm that SiNPs-AuNCs were in a tightly bound state rather than loosely dispersed, TEM images of SiNPs and AuNCs were shown in Fig. 2b and c, respectively. The average diameters of SiNPs and AuNCs were about ~ 2 nm and ~ 3 nm, respectively. The successful formation of SiNPs-AuNCs was also confirmed by TEM imaging in Fig. 2d, which clearly revealed the size of the self-assembled SiNPs-AuNCs at about 20–40 nm. TEM mapping data show that both Si and Au elements are uniformly distributed within the SiNPs-AuNCs (Fig. S4). After the SiNP-AuNC aggregates were successfully formed through self-assembly, the localized interactions within this confined space were likely to alter the charge distribution of AuNCs, thereby changing the localized surface plasmon resonance modes of the particles and producing the AEE enhancement effect. Therefore, we performed a detailed characterization of the surface charge distribution of the aforementioned three types of nanoparticles. As we expected, SiNPs exhibited a positive charge distribution of around + 10 mV, while AuNCs displayed a negative charge distribution of approximately – 40 mV (Fig. S5a, b), which were consistent with our design. After mixing these two at a mass ratio of 10:1 (SiNPs:AuNCs), the aggregated nanoparticles exhibited a zeta potential of – 10 mV (Fig. S5c), indicating that the addition of SiNPs neutralized the charge distribution of the system to a certain extent, accompanied by an approximately 2.3-fold enhancement in the maximum fluorescence emission of AuNCs (Fig. S1e).

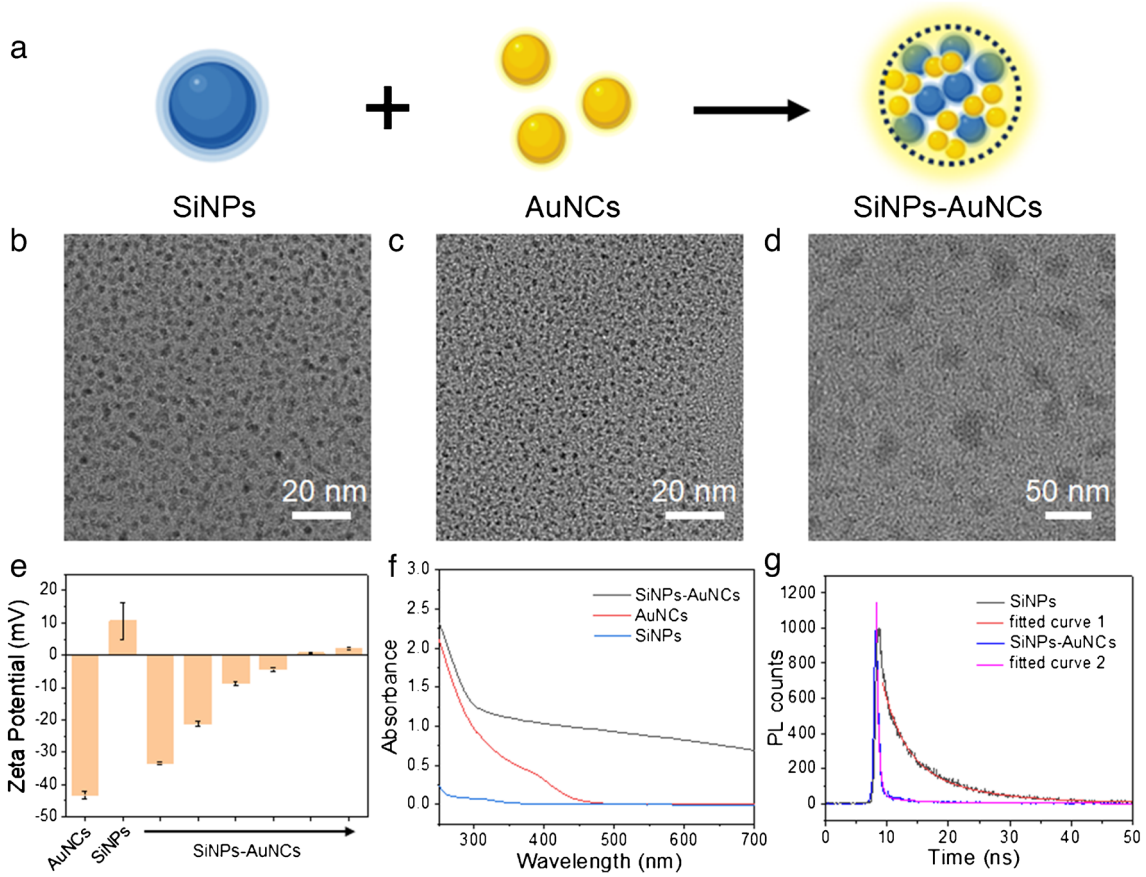

Fig. 2 **a** The scheme of the synthesis of SiNPs-AuNCs. TEM images of **b** SiNPs, **c** AuNCs, and **d** SiNPs-AuNCs. **e** Zeta potential histograms of SiNPs, AuNCs, and different mass ratios of SiNPs-AuNCs (from left to right correspond to the SiNP:AuNC mass ratios of 3:1, 6:1, 10:1, 13:1, 16:1, and 20:1, respectively). **f** UV–vis absorption spectra of SiNPs, AuNCs, and SiNPs-AuNCs at the SiNP:AuNC mass ratios of 3:1. **g** Fluorescence attenuation curves and fitting lines of SiNPs and SiNPs-AuNCs

Additionally, we have performed FTIR analysis on these three materials. As shown in Fig. S6a, the FTIR spectrum of Arg exhibited a broad peak around 3400 cm^{-1}, corresponding to N–H and O–H stretching vibrations. The peak at 1628 cm^{-1} corresponded to C = O stretching vibrations. Peaks in the range of 1400–1500 cm^{-1} (1420, 1475 cm^{-1}) corresponded to N–H bending vibrations, and peaks around 1200 cm^{-1} (1187, 1257 cm^{-1}) corresponded to C-N stretching vibrations. In the FTIR spectrum of Arg-AuNCs, the peaks at 1400–1500 cm^{-1} and 1200–1300 cm^{-1} (corresponding to N–H bending and C-N stretching vibrations, respectively) show slight shifts and changes, indicating that these groups might be involved in the interaction between Arg and AuNCs. Notably, the characteristic peaks of Arg-AuNCs were more similar to those of AuNCs alone (Fig. S6c, blue line), suggesting that Arg interacted with AuNCs primarily through non-covalent interactions. Figure S6b shows that the FTIR spectra of PVP and PVP-AuNCs exhibited corresponding peaks in 2900 cm^{-1} (C-H stretching vibrations), 1650 cm^{-1} (C = O stretching vibrations), and 1400 cm^{-1} and 1100 cm^{-1} (C-N stretching vibrations), indicating that PVP wrapped around AuNCs through physical entanglement, retaining the characteristic peaks of PVP. In the FTIR spectra of SiNPs and SiNPs-AuNCs (Fig. S6c), asymmetric Si–O-Si stretching vibration absorption peaks were observed at 1137 cm^{-1}, along with Si–O bending vibration absorption peaks at 480 cm^{-1}. Additionally, the two major characteristic peaks of GSH-synthesized AuNCs, namely, the N–H stretching vibration peak at 3435 cm^{-1} and the C = O stretching vibration peak at 1640 cm^{-1}, were also detected in the FTIR spectrum of SiNPs-AuNCs. In summary, the comparison of FTIR spectra allowed us to preliminarily infer the assembly and binding modes of the three composites.

Notably, our previous experimental results demonstrated that as the mass ratio of SiNPs to AuNCs in SiNPs-AuNCs aggregates increased from 3:1 to 20:1, the maximum emission peak of AuNCs maintained an enhancing trend. Interestingly, we monitored the surface charge distribution of SiNP-AuNC aggregates under the same conditions and found that with the increase in the proportion of positively

charged SiNPs, the overall zeta potential of the system gradually shifted from negative to positive values (Fig. 2e), without affecting the fluorescence properties of AuNCs (Fig. 1b). Therefore, combined with our previous confirmation that the addition of positively charged L-Arg in the Arg-AuNCs system did not significantly enhance the fluorescence intensity of AuNCs, we could reasonably infer that the AEE fluorescence enhancement mechanism was more likely derived from the enhanced localized surface plasmon resonance (LSPR) effect of AuNCs [30, 31]. Additionally, dynamic light scattering (DLS) analysis of SiNP-AuNC assemblies with different mass ratios (Fig. S7) was performed. At lower ratios, the particle size distribution of SiNP-AuNC assemblies was around 50 nm. At higher ratios, the particle size significantly increased, corresponding to surface charge approaching neutrality (Fig. 2e). Considering the close relationship between nanoparticle size and LSPR, we surmised that the significant size change from individual SiNPs (< 5 nm) to SiNPs-AuNCs (> 20 nm) might also influence the optical properties of SiNPs-AuNCs shown in Fig. 1c. When AuNCs were in an aggregated state with tight spatial confinement, the electron density became locally elevated, promoting the formation of surface plasmons. Moreover, when SiNPs-AuNCs aggregate, a certain gap structure was formed. When the excitation light irradiates this structure, a resonant coupling effect was generated within the gap, increasing the emission probability. Furthermore, the non-radiative transitions of SiNPs, which also possessed luminescent properties, acted on AuNCs under the microstructure of the aggregated particles, leading to the enhancement of AuNC fluorescence emission.

To verify the enhancement of the LSPR effect of AuNCs, we have included the UV–vis absorption spectra of SiNP-AuNC assemblies with mass ratios ranging from 3:1 to 20:1 (Fig. S8a), as well as the spectra of individual SiNPs and AuNCs at equivalent mass concentrations (Fig. S8b, c). Compared to individual SiNPs and AuNCs, the UV–vis spectra of SiNPs-AuNCs assemblies exhibited broader absorption bands, which might be attributed to the increased particle size and changes in the refractive index of the surrounding medium. Additionally, at the SiNP:AuNC mass ratios of 3:1, a significant increase of UV–vis absorption was observed for the SiNP-AuNC system (Fig. 2f), considering the additive nature of absorbance (according to the Beer-Lambert law), the absorbance of SiNPs-AuNCs assemblies at equivalent mass concentrations was significantly higher, particularly at wavelengths above 500 nm, indicating enhanced interactions between nanoparticles. Therefore, the formation of SiNP-AuNC assemblies was accompanied by an enhanced LSPR effect. Furthermore, to verify whether energy transfer occurred from SiNPs to AuNCs, we characterized the excited-state fluorescence lifetimes of SiNPs and SiNPs-AuNCs under the same conditions (Fig. 2g), and τ_{avg} showed a significant decrease from 8.4982 to 2.2211. The above results, to a certain extent, confirmed the resonant coupling effect under the microstructure of SiNP-AuNC aggregates and the energy transfer from SiNPs to AuNCs through non-radiative transitions, collectively contributing to the AEE phenomenon. This emphasized the importance of the aggregation of AuNCs in localized spaces. This aggregated structure enabled the optical properties of AuNCs and SiNPs to be tuned by modulating the aggregation mode and interactions, providing a theoretical basis and experimental support for designing high-performance dual-emission fluorescent biosensors.

Establishment of dual-emission ratiometric fluorescence detection assay

Based on the above research, we further applied this probe to establish a dual-emission ratiometric fluorescence detection biosensing system. SiNPs played a performance-regulating role, effectively inducing the AEE process of AuNCs, thereby amplifying the weak fluorescence signal of AuNCs. Additionally, SiNPs themselves also possessed fluorescence emission properties. Therefore, the SiNP-AuNC system as a probe could achieve dual emission under single-wavelength excitation. This provided the possibility for constructing ratiometric fluorescence biosensors. Compared to single AuNCs, dual-emission ratiometric detection could effectively eliminate the influence of external environmental noise and probe concentration fluctuations, enabling more stable and reliable quantitative analysis [32]. Herein, we aimed to establish a classical dual-emission ratiometric detection system for BLM detection by optimizing the properties of SiNP-AuNC nanoprobes, overcoming potential interferences in complex biological sample analysis (Fig. 3a).

First, we conducted a feasibility study on the dual-emission ratiometric fluorescence detection assay. In the system of SiNPs only, the addition of Cu^{2+} and/or BLM did not interfere with the fluorescence emission curve of SiNPs (Fig. 3b). In the system containing only AuNCs, the addition of Cu^{2+} significantly reduced the fluorescence intensity of the characteristic peak of AuNCs, while the fluorescence intensity almost completely recovered after the addition of BLM. Combining the results from these two sets of experiments, in the SiNPs-AuNCs system under single-wavelength excitation, the fluorescence of SiNPs remained unaffected by Cu^{2+} and/or BLM, serving as a reliable reference signal. The fluorescence of AuNCs, as the detection signal, retained its sensitive response to Cu^{2+} and BLM (Fig. 3c, d).

To establish a robust and reliable ratiometric fluorescence biosensing platform, the SiNP-AuNC nanoprobes were systematically optimized under various conditions. First, the temperature dependence of the ratiometric signal

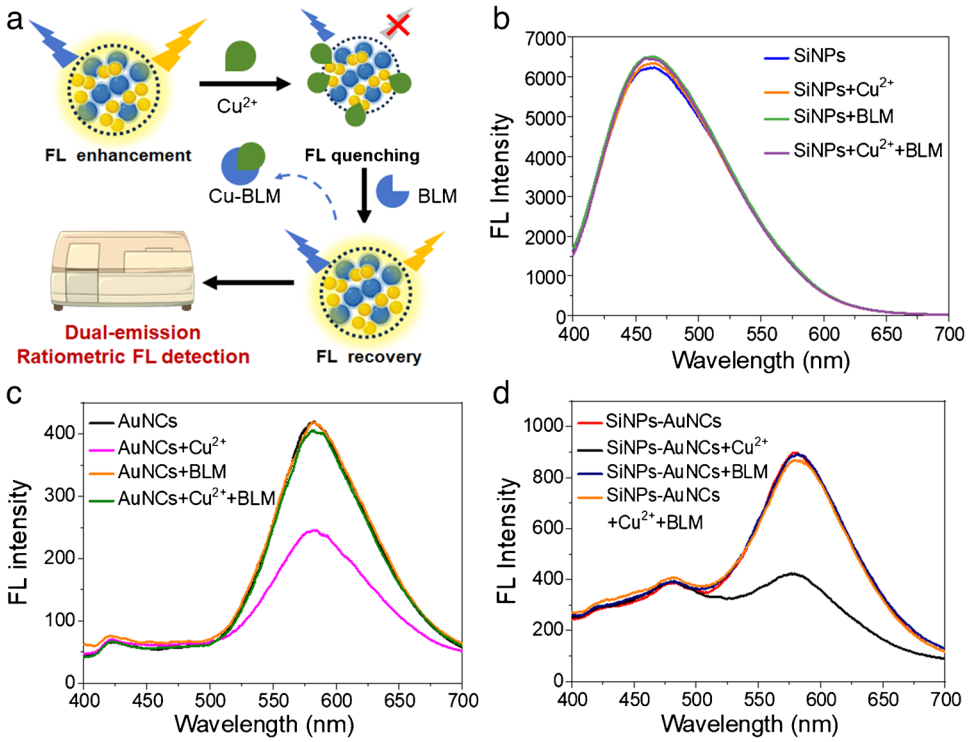

Fig. 3 **a** The scheme of dual-emission ratiometric fluorescence detection sensors. **b** Fluorescence spectra of SiNPs in the presence of Cu^{2+} and/or BLM. **c** Fluorescence spectra of AuNCs in the presence of Cu^{2+} and/or BLM. **d** Fluorescence spectra of SiNPs-AuNCs in the presence of Cu^{2+} and/or BLM

was investigated over a range of 25–45 °C. As depicted in Fig. S9a, the ratiometric response remained relatively consistent across the evaluated temperatures. Furthermore, the temporal stability of the ratiometric signal was assessed upon the addition of different Cu^{2+} concentrations. As shown in Fig. S9b, the ratiometric intensities exhibited a gradual decrease over time, eventually stabilizing after approximately 10 min. Finally, the pH dependence of the ratiometric response was evaluated under both Cu^{2+}-quenched and BLM-recovered conditions (Fig. S9c). The ratiometric intensities remained relatively constant across a broad pH range from 6.0 to 8.5, demonstrating the robustness of the SiNP-AuNC nanoprobes in maintaining their sensing capabilities under varying pH conditions. This pH-insensitive behavior was particularly advantageous for biological sample analysis, where fluctuations in sample pH were commonly encountered. Through these systematic optimizations, the SiNP-AuNC nanoprobes exhibited excellent operational stability and minimal susceptibility to environmental interferences, thereby ensuring reliable and accurate ratiometric fluorescence detection in complex biological matrices.

Fluorescence-enhanced dual-emission ratiometric probe for BLM detection

Based on verifying the feasibility of the SiNP-AuNC sensing system, we constructed a dual-emission ratiometric biosensor for BLM detection. As shown in Fig. 4a, the SiNP-AuNC nanoprobe exhibited dual emission peaks at 480 nm and 580 nm under 365 nm excitation. Upon the addition of a certain concentration of Cu^{2+}, a significant quenching phenomenon of the AuNCs emission peak at 580 nm was observed. This was due to the specific binding of Cu^{2+} to the thiol groups on the surface of AuNCs, triggering the fluorescence quenching of AuNCs. It was noteworthy that even when the Cu^{2+} concentration increased to 10 μM, the fluorescence emission intensity of SiNPs at 480 nm remained unchanged. Based on the changes of the dual-peak ratio of 580/480 nm, we successfully established a correlation curve between Cu^{2+} concentration with fluorescence ratio (Fig. 4b). A good linear correlation ($R^2 = 0.9665$) was observed when the Cu^{2+} concentration was below 4 μM. Therefore, subsequent detection experiments selected 4 μM of Cu^{2+} as the fluorescence suppression concentration. Additionally, we investigated the fluorescence quenching effect of SiNPs-AuNCs in the presence of varying concentrations of the fluorophore/quencher (i.e., SiNPs-AuNCs and Cu^{2+} ions). The experimental results indicate that the Stern–Volmer plot exhibits nonlinear behavior with an initial upward curvature, deviating from the linear plot predicted by the classical Stern–Volmer equation (Fig. S10). This suggests the coexistence of both static and dynamic quenching processes. We have fitted the data using the modified Stern–Volmer equation $I_0/I = (1 + K_d[Q]) \cdot (1 + K_s[Q])$, where I_0 and I represent the fluorescence intensity in the absence and presence of the quencher, respectively. Here, K_d is the dynamic quenching constant, and K_s is the static quenching constant. The

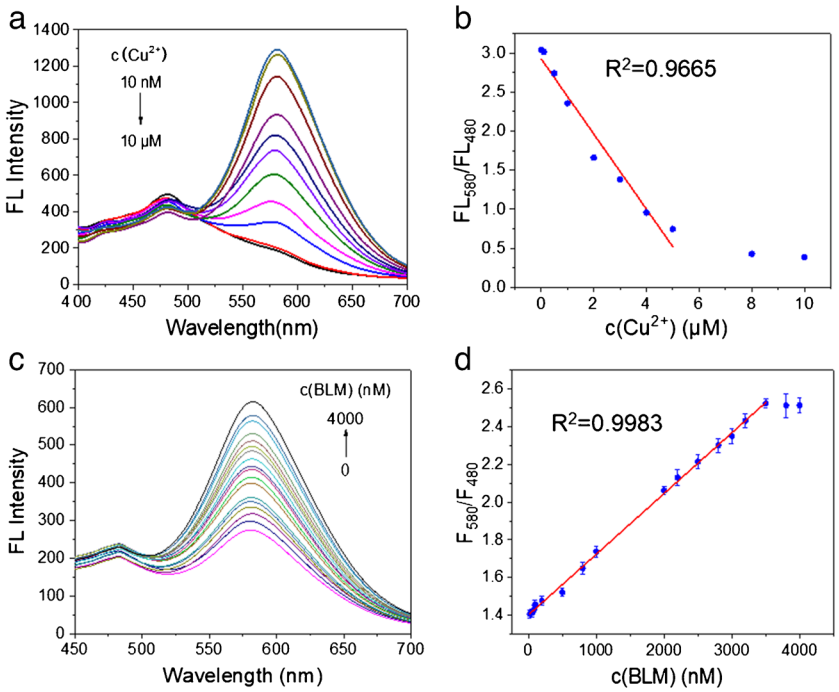

Fig. 4 **a** Fluorescence spectra of SiNPs-AuNCs in the presence of various Cu^{2+} (10 nM–10 μM) and **b** plot of the relationship between the fluorescence intensity ratio F_{580}/F_{480} and Cu^{2+} concentrations. **c** Fluorescence spectra of SiNPs-AuNCs in the presence of various BLM concentrations (0–4000 nM) and **d** plot of the relationship between the fluorescence intensity ratio F_{580}/F_{480} and BLM concentrations

fitted equation obtained was $I_0/I = (1 + 0.0440[Q]) \cdot (1 + 0.4241[Q])$, which showed a strong correlation ($R^2 = 0.9941$).

Furthermore, we investigated the detection of BLM using the SiNP-AuNC system. As shown in Fig. 4c, with increasing BLM concentration, the AuNC fluorescence emission peak at 580 nm gradually recovered, while the SiNP peak intensity at 480 nm remained stable. This process could be attributed to the competitive binding between Cu^{2+} and BLM. In the presence of BLM, due to its strong affinity for Cu^{2+}, it could effectively remove Cu^{2+} from the surface of AuNCs, restoring the fluorescence at 580 nm. A good linear detection range was obtained using the dual-emission ratiometric method (Fig. 4d), extending up to 0–3.5 μM, and the linear correlation between Cu^{2+} concentration and fluorescence ratio was excellent ($R^2 = 0.9983$). The detection limit of BLM was estimated to be 35.27 nM according to the 3σ rule. These results demonstrated that the current method was more sensitive compared to most of the previous reported methods (Table S1). This ratiometric sensing system successfully overcame the limitations of AuNC-based biosensing, significantly improving detection time and linear detection range.

Selectivity and anti-interference performance of the proposed sensing approach

To evaluate the selectivity and anti-interference capability of the proposed sensing strategy, we conducted interference tests on coexisting metal ions and biological small molecules that the SiNP-AuNC nanoprobes might encounter. First, apart from Cu^{2+}, nine other metal ions (Na^+, K^+, Mg^{2+}, Al^{3+}, Ca^{2+}, Zn^{2+}, Hg^{2+}, Pb^{2+}, and Cd^{2+}) at a concentration of 200 μM did not significantly affect the dual-emission ratio of 580 nm/480 nm (Fig. S11a). This result fully demonstrated the excellent selectivity of the constructed system for metal ions. Second, except for BLM, common biological small molecules (dopamine, ascorbic acid, glucose, L-glutamic acid, aspartic acid, L-cysteine, L-tyrosine, and L-histidine) at the concentration of 200 μM did not cause significant changes in the 580 nm/480 nm ratio (Fig. S11b). This further verified that this proposed dual-emission system possessed outstanding anti-interference ability, effectively eliminating the interference of impurity molecules in complex biological matrices, laying the foundation for achieving highly selective and sensitive biomolecule detection. In summary, through selectivity and anti-interference assessments, the SiNP-AuNC nanoprobes exhibited excellent analytical performance, enabling reliable and precise detection of specific analytes in complex biological environments.

Application of the SiNP-AuNC sensing system in real sample analysis

To validate the practical applicability of the proposed SiNP-AuNC sensing system, we employed the standard addition method to determine BLM concentrations in serum samples. To assess the recovery and precision of the method, we spiked the serum samples with different concentrations of BLM (500 nM, 1500 nM, and 2500 nM). As shown in Table S2, the recoveries of BLM ranged from

96.80 to 105.9%, with relative standard deviations (RSD) varying from 3.17 to 4.24%. These results demonstrated the reliability and accuracy of the proposed method for BLM quantification in complex biological matrices.

The satisfactory recovery and precision could be attributed to several factors. First, the dual-emission ratiometric sensing strategy effectively minimized the influence of external environmental fluctuations and sample matrix effects, ensuring the robustness of the method. Second, the AEE mechanism of the SiNPs-AuNCs nanoprobes significantly amplified the fluorescence signal, leading to improved sensitivity and reproducibility. Lastly, the high selectivity and anti-interference capability of the sensing system, as demonstrated in the previous sections, contributed to the accurate determination of BLM in the presence of various interfering substances commonly found in serum samples.

Conclusion

This research elucidates the fundamental mechanistic factors that dictate the AEE of AuNCs when subjected to spatial confinement. Systematic investigations demonstrated intimate interparticle proximity and optimal surface charge density as crucial for efficient AEE. Significantly, the construction of SiNP-AuNC nanoprobes optimized the AEE process while enabling a dual-emission ratiometric sensing strategy. This innovative nanoprobe synergistically harnesses AEE and the stable reference emission from SiNPs, overcoming weak AuNC fluorescence and environmental susceptibility. Exhibiting exceptional operational stability, pH/temperature resilience, and remarkable selectivity, the SiNPs-AuNCs nanoprobes achieved highly sensitive and linear BLM detection, outperforming conventional single-emission AuNC sensors. The sensor platform unlocks AEE's potential for AuNC-based biosensing by integrating spatial confinement, ratiometric detection, and SiNPs' unique optics. The mechanistic insights of dual-emission ratiometric nanoprobes represent significant advancements, paving the way for rational design of high-performance sensing systems tailored for complex biological environments and expanding AuNC-based bioanalytical frontiers.

Supplementary Information The online version contains supplementary material available at https://doi.org/10.1007/s00604-024-06530-x.

Funding This work was financially supported by the National Natural Science Foundation of China (22304100 and 22207062), Natural Science Foundation of Shandong Province (ZR2022QB223 and ZR2022QB209), and Open Project of State Key Laboratory of Chemo/Biosensing and Chemometrics of Hunan University (HNUKJ20230072). Cartoons in Schemes were created with BioRender software.

Data availability The authors confirm that the data supporting the findings of this study are available within the article and/or its supplementary materials.

Declarations

Ethical approval The authors confirm that all serum assay procedures were conducted in strict accordance with the guidelines established by the regional ethics committee for animal experiments at Qufu Normal University Institutional Animal Care and Use (2023026).

Conflict of interest The authors declare no competing interests.

References

1. Zheng Y, Lai L, Liu W, Jiang H, Wang X (2017) Recent advances in biomedical applications of fluorescent gold nanoclusters. Adv Colloid Interface Sci 242:1–16
2. Zhang C, Gao X, Chen W, He M, Yu Y, Gao G, Sun T (2022) Advances of gold nanoclusters for bioimaging. iScience 25(10):105022
3. Halawa MI, Lai J, Xu G (2018) Gold nanoclusters: synthetic strategies and recent advances in fluorescent sensing. Mater Today Nano 3:9–27
4. Li Y, Zhai T, Chen J, Shi J, Wang L, Shen J, Liu X (2022) Water-dispersible gold nanoclusters: synthesis strategies, optical properties, and biological applications. Chemistry 28(10):e202103736
5. Khan IM, Niazi S, Yue L, Zhang Y, Pasha I, Iqbal Khan MK, Akhtar W, Mohsin A, Chughati MFJ, Wang Z (2022) Research update of emergent gold nanoclusters: a reinforced approach towards evolution, synthesis mechanism and application. Talanta 241:123228
6. Yan X, Wang T, Li H, Zhang L, Xin H, Lu G (2022) Flexible aggregation-induced emission-active hydrogel for on-site monitoring of pesticide degradation. ACS Nano 16(11):18421–18429
7. Zhang W, Jiang X, Wu Y, Jiang J, Liu X, Liu Y, Wang W, Lai J, Wang X (2023) Zeolitic imidazolate framework-8 encapsulating gold nanoclusters and carbon dots for ratiometric fluorescent detection of adenosine triphosphate and cellular imaging. Talanta 255:124226
8. You J-G, Lu C-Y, Krishna Kumar AS, Tseng W-L (2018) Cerium (III)-directed assembly of glutathione-capped gold nanoclusters for sensing and imaging of alkaline phosphatase-mediated hydrolysis of adenosine triphosphate. Nanoscale 10(37):17691–17698
9. Yu Y, Li J, Chen T, Tan YN, Xie J (2015) Decoupling the co-reduction protocol to generate luminescent Au 22 (SR) 18 nanocluster. J Phy Chem C 119:10910–10918
10. Pinto A, Svahn N, Lima JC, Rodríguez L (2017) Aggregation induced emission of gold (I) complexes in water or water mixtures. Dalton Trans 46(34):11125–11139
11. Qing T, He X, He D, Qing Z, Wang K, Lei Y, Liu T, Tang P, Li Y (2016) Oligonucleotide-templated rapid formation of fluorescent gold nanoclusters and its application for Hg^{2+} ions sensing. Talanta 161:170–176
12. Dou X, Yuan X, Yu Y, Luo Z, Yao Q, Leong DT, Xie J (2014) Lighting up thiolated Au@Ag nanoclusters *via* aggregation-induced emission. Nanoscale 6(1):157–161
13. Peng H, Huang Z, Deng H, Wu W, Huang K, Li Z, Chen W, Liu J (2020) Dual enhancement of gold nanocluster electrochemiluminescence: electrocatalytic excitation and aggregation-induced emission. Angew Chem Int Ed 59(25):9982–9985
14. Tian R, Yan D, Li C, Xu S, Liang R, Guo L, Wei M, Evans DG, Duan X (2016) Surface-confined fluorescence enhancement of Au

nanoclusters anchoring to a two-dimensional ultrathin nanosheet toward bioimaging. Nanoscale 8(18):9815–9821
15. Cao F, Ju E, Liu C, Li W, Zhang Y, Dong K, Liu Z, Ren J, Qu X (2017) Encapsulation of aggregated gold nanoclusters in a metal–organic framework for real-time monitoring of drug release. Nanoscale 9(12):4128–4134
16. Wang T, Jiang K, Wang Y, Xu L, Liu Y, Zhang S, Xiong W, Wang Y, Zheng F, Zhu J-J (2024) Prolonged near-infrared fluorescence imaging of micrornas and proteases *in vivo* by aggregation-enhanced emission from DNA-AuNC nanomachines. Chem Sci 15(5):1829–1839
17. Chen X, Li G, Yue X, Peng C, Wang J (2023) Ratiometric fluorescent detection of carbendazim in foods based on metallic nanoclusters self-assembled nanocomplex. Food Chem 424:136478
18. Zhu H, Zhou Y, Wang Y, Xu S, James TD, Wang L (2022) Stepwise-enhanced tumor targeting of near-infrared emissive Au nanoclusters with high quantum yields and long-term stability. Anal Chem 94(38):13189–13196
19. Guo Y, Zhang J, Liu J, Wang N, Su X (2023) A highly sensitive fluorescence "on-off-on" sensing platform for captopril detection based on AuNCs@ZIF-8 nanocomposite. Anal Chim Acta 1276:341649
20. Chen Z-J, Wu H-L, Shen Y-D, Wang H, Zhang Y-F, Hammock B, Li Z-F, Luo L, Lei H-T, Xu Z-L (2022) Phosphate-triggered ratiometric fluoroimmunoassay based on nanobody-alkaline phosphatase fusion for sensitive detection of 1-naphthol for the exposure assessment of pesticide carbaryl. J Hazard Mater 424:127411
21. Ma J, Yang M, Zhang B, Niu M (2024) The roles of templates consisting of amino acids in the synthesis and application of gold nanoclusters. Nanoscale 16(15):7287–7306
22. Li S, Zhang H, Huang Z, Jia Q (2024) Fluorometric and colorimetric dual-mode sensing of α-glucosidase based on aggregation-induced emission enhancement of AuNCs. J Mater Chem B 12(6):1550–1557
23. Chen P-W, Tseng C-Y, Shi F, Bi B, Lo Y-H (2019) Measuring electric charge and molecular coverage on electrode surface from transient induced molecular electronic signal (TIMES). Sci Rep 9(1):16279
24. Tavakkoli Yaraki M, Rubio NS, Tukova A, Liu J, Gu Y, Kou L, Wang Y (2024) Spectroscopic identification of charge transfer of thiolated molecules on gold nanoparticles *via* gold nanoclusters. J Am Chem Soc 146(9):5916–5926
25. Haye L, Diriwari PI, Alhalabi A, Gallavardin T, Combes A, Klymchenko AS, Hildebrandt N, Le Guével X, Reisch A (2023) Enhancing near infrared ii emission of gold nanoclusters *via* encapsulation in small polymer nanoparticles. Adv Opt Mater 11(11):2201474
26. Zhong Y, Zhang J, Li T, Xu W, Yao Q, Lu M, Bai X, Wu Z, Xie J, Zhang Y (2023) Suppression of kernel vibrations by layer-by-layer ligand engineering boosts photoluminescence efficiency of gold nanoclusters. Nat Commun 14(1):658
27. Yuan P, Zhang H, Zhou Y, He T, Malola S, Gutiérrez-Arzaluz L, Li Y, Deng G, Dong C, Huang R, Song X, Teo BK, Mohammed OF, Häkkinen H, Bakr OM, Zheng N (2024) Thermally activated delayed fluorescence Au-Ag-oxo nanoclusters: from photoluminescence to radioluminescence. Aggregate 5(2):e475
28. Li Y, Teng S, Wang M, Duan B, Huang Z (2021) Molecular crowding-modulated fluorescence emission of gold nanoclusters: ligand-dependent behaviors and application in improved biosensing. Sens Actuators B Chem 330:129290
29. You J-G, Tseng W-L (2019) Peptide-induced aggregation of glutathione-capped gold nanoclusters: a new strategy for designing aggregation-induced enhanced emission probes. Anal Chim Acta 1078:101–111
30. Niu R, Gao F, Wang D, Zhu D, Su S, Chen S, YuWen L, Fan C, Wang L, Chao J (2022) Pattern recognition directed assembly of plasmonic gap nanostructures for single-molecule SERS. ACS Nano 16(9):14622–14631
31. Park S, Kim H, Lim SC, Lim K, Lee ES, Oh KT, Choi H-G, Youn YS (2019) Gold nanocluster-loaded hybrid albumin nanoparticles with fluorescence-based optical visualization and photothermal conversion for tumor detection/ablation. J Control Release 304(28):7–18
32. Yu F, Xiang H, He S, Zhao G, Cao Z, Yang L, Liu H (2022) Gold nanocluster-based ratiometric fluorescent probe for biosensing of Hg^{2+} ions in living organisms. Analyst 147(12):2773–2778